Adaptive Nonlinear Least Squares Framework for Contactless Vital Sign Monitoring

Gabriel Beltrão, *Graduate Student Member, IEEE*, Wallace A. Martins, *Senior Member, IEEE*, Bhavani Shankar M. R., *Senior Member, IEEE*, Mohammad Alaee-Kerahroodi, *Member, IEEE*, Udo Schroeder, and Dimitri Tatarinov

***Abstract*— The respiratory and heart rates are critical physiological parameters, and conventional contact-based monitoring techniques may cause discomfort and epidermal damage, being therefore inadequate for long-term monitoring. Despite recent advances, accurate contactless vital sign monitoring is still challenging in practical scenarios, especially in relation to heart rate estimation. In this work, we propose a comprehensive framework for vital sign processing in frequency-modulated continuous-wave radar systems and evaluate its performance with real data imitating common working conditions in an office environment. First, to improve the signal-to-noise ratio before estimation, we propose a novel slow-time phase correlation processing, which allows early integration of the vital sign energy at nearby range bins. Subsequently, we present an adaptive nonlinear least squares framework that explores the harmonic structure existing in the recovered displacement signal. An additional Kalman filter stage is designed to select among multiple estimates from different search regions, thus conferring adaptivity and robustness against harmonic interference and noise. This approach largely provides estimates within the predefined error intervals, being capable of tracking the true breathing and heart rate values even during continuous small body movements. The final accuracy and root mean square error values have shown enhanced estimation, outperforming conventional spectral estimation and other recently proposed methods in almost all scenarios.**

***Index Terms*— Breathing rate, frequency-modulated continuous-wave (FMCW), harmonics, heart rate, mm-wave, radar, random body movements, vital signs.**

I. Introduction

PEOPLE are living longer. Between 2015 and 2050, the proportion of the world's population over 60 years will nearly double and outnumber children under the age of 5 [1]. Due to the rapid aging of the population worldwide, a lot of effort is being dedicated to providing efficient and more accessible healthcare solutions.

In this context, continuous monitoring of vital signs plays a crucial role in the early detection of conditions that affect the well-being of a patient. The respiratory and heart rates are critical physiological parameters, and by continuously monitoring this information, it is possible to detect drowsiness [2], sleep apnea [3], and even depression [4]. However, conventional monitoring devices, usually connected by cables, besides restricting mobility, may cause discomfort and epidermal damage, being therefore inadequate for long-term monitoring.

On the other hand, contactless radar-based vital sign monitoring provides several advantages over standard devices. Unlike cameras, radar signals can penetrate through different materials and are not affected by skin pigmentation or ambient light levels [5]. Unlike wearable sensors, radar systems do not require users to wear or carry any additional equipment. In addition, radar devices preserve privacy [6] and can be low power and low cost. These inherent characteristics have drawn the attention of the research community, and a variety of radar types are now being used to address different healthcare applications, including sleep monitoring [7], life detection and rescue [8], assisted living [9], diagnosis [10], and many others.

Continuous-wave (CW) radars have been extensively employed for vital sign monitoring [11], [12], [13]. These devices have the advantages of low transmitted power, simple hardware structure, and high sensitivity, which explains their widespread use across various areas. Within this group, unmodulated CW systems have the simplest architecture but with the limitation that no distance information in relation to the target is acquired. In addition, other moving objects may interfere with the CW radar signal, making it more difficult to isolate the target information from interfering objects [6]. For being able to estimate the target distance (range), typical approaches use ultrawideband (UWB) and frequency-modulated continuous-wave (FMCW) radars. Recently, the application of millimeter-wave FMCW radars to short-range vital sign monitoring has been widely investigated [14], [15], [16]. Such radars benefit from high range resolution and Doppler sensitivity, yet with simple architecture, which allows using relatively simple circuits and low-cost analog-to-digital converters (ADCs) [17]. Furthermore, the mass production from the automotive industry has resulted in the

Manuscript received 12 September 2022; revised 22 October 2022; accepted 25 October 2022. Date of publication 29 November 2022; date of current version 4 April 2023. This work was supported by the Luxembourg National Research Fund (FNR) under the FNR Industrial Fellowship Grant through Project MIDIA under Grant 14269859. *(Corresponding author: Gabriel Beltrão.)*

This work involved human subjects or animals in its research. The authors confirm that all human/animal subject research procedures and protocols are exempt from review board approval.

Gabriel Beltrão, Wallace A. Martins, Bhavani Shankar M. R., and Mohammad Alaee-Kerahroodi are with the Interdisciplinary Centre for Security, Reliability and Trust (SnT), University of Luxembourg, 4365 Esch-sur-Alzette, Luxembourg (e-mail: gabriel.tedgue-beltrao@uni.lu).

Udo Schroeder and Dimitri Tatarinov are with IEE S.A., 7795 Bissen, Luxembourg (e-mail: udo.schroeder@iee.lu).

Color versions of one or more figures in this article are available at https://doi.org/10.1109/TMTT.2022.3222384.

Digital Object Identifier 10.1109/TMTT.2022.3222384

large availability of inexpensive radar modules with increased capabilities and functionalities [18].

Despite recent advances, accurate vital sign monitoring is still challenging in practical scenarios, especially in relation to heart rate estimation. Radar-based vital sign processing relies on the phase analysis of the backscattered signal, corresponding to the chest wall's periodic displacement due to the breathing and heartbeat mechanisms. The recovered displacement signal is usually composed not only of the breathing and heartbeat fundamental frequencies but also of their associated harmonics. The challenge stems from the fact that the tiny heartbeat-induced motion is typically several times smaller than the one originated from breathing. Therefore, the heartbeat signal can be easily buried in the background noise or masked by the higher order harmonics of the breathing signal. This harmonic interference in the heartbeat signal has been extensively reported as one of the main issues in radar-based vital sign monitoring [19], [20], [21], [22], and as discussed in [23], depending on the signal-to-interference ratio (SIR) and the specific combination of fundamental breathing/heartbeat frequencies, most techniques fail to provide robust heart rate estimation. Furthermore, additional frequency components and intermodulation products may also be present in the recovered signal, originated from different sources including radar nonlinearities, phase-demodulation issues [24], and random body movements from the monitored subject [25]. These interfering elements tend to be dominant in the neighborhood of the heartbeat's fundamental frequency, often preventing detection and hindering estimation.

In this article, we propose a comprehensive framework for vital sign processing based on a millimeter-wave FMCW radar system, and we evaluate its performance using real data collected while imitating typical working conditions in an office environment. First, to improve the signal-to-noise ratio (SNR) before estimation, we propose a novel slow-time phase correlation processing, which allows for the integration of displacement signals at nearby range bins, while still preserving its relevant frequency content. Early integration of these correlated signals allows useful exploitation of the vital sign energy, without the need of processing each range bin independently, as suggested in [26]. Subsequently, we present an adaptive nonlinear least squares (ANLS) framework that explores the harmonic structure existing in the recovered displacement signal. For estimating the breathing rate, we simplify the nonlinear least squares (NLS) algorithm recently proposed in [27] and [28] and adaptively adjust the search region over the NLS objective function according to previous estimates from adjacent processing windows. For the heart rate estimation, we extend the basic NLS approach, and to avoid harmonic interference from breathing, we explore the original idea in [29] by generating multiple heart rate estimates based on the heartbeat's own harmonics. However, it is impossible to know which of these estimates is reliable, and to overcome this, we designed an additional Kalman filter stage that uses the gating process (based on its own prediction) to select the best heart rate estimate, thus avoiding low-SNR, ambiguous or harmonic-interfered candidates. Due to the efficient NLS implementation, based on the fast Fourier transform (FFT), the proposed method can overcome the SNR limitations reported in [29], without significantly increasing the computational burden.

The remainder of this article is organized as follows. In Section II, we introduce the basic operational principle and system modeling for contactless radar-based vital sign monitoring using FMCW radars. The signal processing framework is presented in Section III, whereas, in Section IV, we describe our proposal for robust and accurate breathing and heartbeat frequency estimation. Finally, Section V presents some experimental results. In Section VI, the conclusions are drawn.

A. Notations

Throughout this article, we are adopting the following notation: lower case boldface for vectors $\boldsymbol{x}$ and upper case boldface for matrices $\boldsymbol{X}$. The letter j represents the imaginary unit (i.e., $j = (-1)^{1/2}$), with the absolute value and angle operators given by the symbols $|(\cdot)|$ and $\angle(\cdot)$. The transpose, conjugate, and conjugate transpose operators are denoted, respectively, by the symbols $(\cdot)^T$, $(\cdot)^*$, and $(\cdot)^H$. The sets of N-dimensional vectors of complex and real numbers are represented by $\mathbb{C}^N$ and $\mathbb{R}^N$. The Euclidean norm of the vector $\boldsymbol{x}$ is denoted by $||\boldsymbol{x}||$. The identity matrix, with size determined from the context, is denoted by $\boldsymbol{I}$. For any complex number x, we use $\Re$ and $\Im$ to denote, respectively, the real and the imaginary parts of x. We are using the acronym "bpm" alternatively as breaths per minute (breathing rate) or beats per minute (heart rate). The meaning will be clear from the context.

II. System Modeling

Fig. 1 shows the basic operational principle of contactless radar-based vital sign monitoring. The transmitted FMCW signal can be written as

$$x_T(t) = \sqrt{A_T}\cos\left(2\pi f_c t + \pi\frac{B}{T_p}t^2 + \phi(t)\right) \tag{1}$$

where A_T is the transmitted power, f_c is the operating frequency (initial frequency of the chirp), B is the pulse bandwidth, T_p the pulse duration, and $\phi(t)$ is the transmitter's phase noise (local oscillator). When we breathe, or when the heart beats, the subtle chest wall motion modulates the FMCW signal, which is reflected with additional phase information related to this movement. Ideally, the radar receives a scaled and shifted version of the transmitted signal given by [18]

$$x_R(t) = \alpha\sqrt{A_T}\cos\left(2\pi f_c(t - t_d) + \pi\frac{B}{T_p}(t - t_d)^2 + \phi(t - t_d)\right) \tag{2}$$

where α represents an attenuation coefficient and $t_d = 2r(t)/c$ is the range-dependent time delay from a given object at radial range $r(t)$, with c being the speed of light. The received signal is mixed with a replica of the transmitted signal, and after quadrature demodulation, it can be approximated as

$$x_\psi(t) = A_\psi e^{j\left(2\pi f_\psi t + \Delta\theta(t) + \Delta\phi(t)\right)} \tag{3}$$

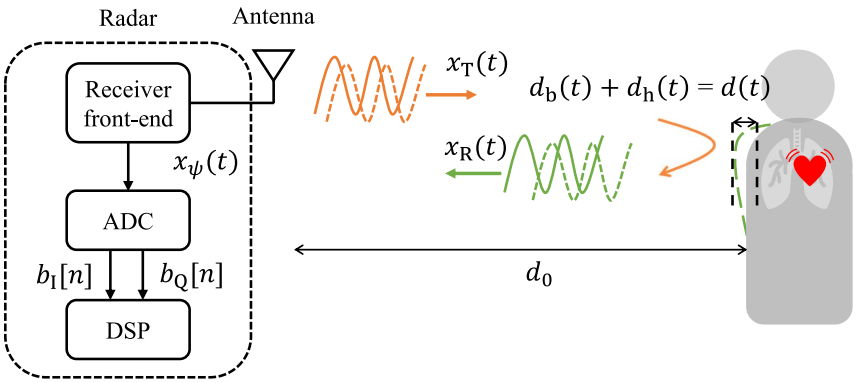

Fig. 1. Contactless radar-based vital sign monitoring. Basic operational principle. For simplicity, a single ADC channel is shown.

which represents the beat signal, where A_ψ is the beat signal amplitude, f_ψ is the beat frequency, and

$$\Delta\theta(t) = 2\pi f_c t_d + \pi \frac{B}{T_p} t_d^2 \tag{4}$$

is the time-varying phase relative to the movement of the monitored subject. The amplitude terms in (2) and (3) may vary slightly according to the chest vibration. However, as we are interested in the phase of the slow-time signal, this small variation has no implications, and it is often neglected in the literature [18], [24], [30]. In addition, due to the range-correlation effect [31], the residual phase noise $\Delta\phi(t)$ in (3) is usually neglected for short-range applications. Furthermore, the term $\pi(B/T_p)t_d^2$ in (4) can also be discarded as it is negligibly small in practical scenarios [18]. Finally, for an object at nominal range d_0, we have

$$\Delta\theta(t) = \frac{4\pi r(t)}{\lambda_c} = \frac{4\pi d_0}{\lambda_c} + \frac{4\pi d(t)}{\lambda_c} \tag{5}$$

where $\lambda_c = 1/f_c$ is the operating wavelength, and ideally, $d(t)$ would correspond exclusively to the chest wall movement, which is assumed to be the superposition of those induced by breathing and heartbeat. In this case, we can finally write

$$\Delta\theta(t) = \frac{4\pi(d_0 + d_b(t) + d_h(t))}{\lambda_c} \tag{6}$$

with $d_b(t)$ and $d_h(t)$ being the displacements due to breathing and heartbeat, respectively. These movements involve multiple patterns of motion, not only from the chest wall surface but also from the belly, shoulders, and back [32], [33]. Different models have already been proposed for representing these signals from simple sinusoidal approximations [29], [34] to more complicated patterns as described in [35] and [36]. Perfect recovery of the chest wall displacement $d(t)$ would allow precise estimation of breathing and heartbeat frequencies by analyzing the periodicity of the signal. However, in practical applications, besides unavoidable hardware imperfections, the received radar signal is usually mixed with additional reflections from the external environment, arising not only from different body movements of the monitored subject but also from every object in the radar's field of view. These interfering signals are usually much stronger than those induced by the chest wall millimeter displacement, and this makes accurate recovery and subsequent estimation of the breathing and heartbeat frequencies a challenging task.

III. Vital Sign Processing

Fig. 2 shows the signal processing block diagram of the proposed solution for contactless vital sign monitoring. For providing sufficient SNR, while still preserving the update rate, this processing is commonly performed using overlapped sliding windows. This strategy leaves sufficient time to acquire several breathing/heartbeat cycles, revealing (and enhancing) the periodicity of the movement. Hence, the obtained frequency value from each processing window corresponds to an average over the window duration. In addition, the frequency resolution is also improved. In order to provide new estimates every one or two seconds, large overlaps are usually employed.

The preprocessing block receives the baseband radar signals as in-phase and quadrature samples ($b_I[n]$ and $b_Q[n]$) from the ADCs. In order to extract the slow-time signal from the monitored subject at a specific range and angle position, we use a 2-D discrete Fourier transform (DFT) over the radar data cube, across the range and angle dimensions. Given our specific conditions of monitoring, the detector can be implemented by simply looking for the slow-time signal at the range/angle bin with greater energy.

Phase demodulation is essentially the process where the complex samples of the slow-time signal will be combined with the aim to recover the displacement signal containing the phase information relative to the chest wall movement over time. Several techniques have been already proposed for that, including the complex-signal demodulation (CSD) [37], [38], [39] and the linear demodulation [4], [40], [41]. As discussed in [23], [42], and [43], these methods suffer from intermodulation products and harmonic interference when applied at higher operating frequencies. To avoid these issues and enable precise phase recovery, the arctangent demodulation (AD) [10], [24], [44] is being used in this work. The recovered displacement signal can, thus, be obtained as

$$\hat{d}[n] = \frac{\lambda_c}{4\pi} \cdot \text{unwrap}\left(\arctan\left[\frac{\Im(s[n])}{\Re(s[n])}\right]\right) \tag{7}$$

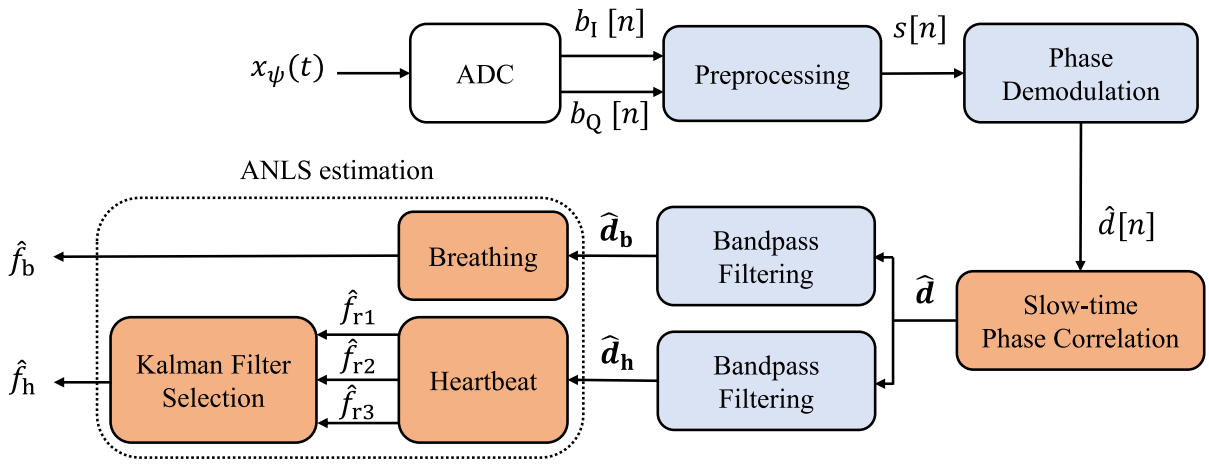

Fig. 2. Block diagram of the proposed signal processing chain.

where $s[n]$ represents the samples of the complex slow-time signal at the target range bin. The unwrap operation is necessary for removing possible phase discontinuities caused by the bounded image of the arctangent function. Due to the high sensitivity of mm-wave devices, wrapped phases around $[-\pi, \pi]$ are expected when actual displacements are larger than $\lambda_c/4$.

Prior to the AD, possible dc offsets must be compensated, and for this, we use the Levenberg–Marquardt (LM) algorithm, which provides a maximum likelihood estimate for this problem [45]. For removing any residual dc values and possible high-frequency noise components, the recovered displacement signal is filtered using a bandpass Kaiser window ($\beta = 6.5$) from 0.1 to 3 Hz (6–180 breaths/minute) for the breathing and 0.5 to 5 Hz (30–300 beats/minute) for the heartbeat. This corresponds to the physiological range of fundamental frequencies, including a few possible harmonics. The bandpass filtered signals $\hat{\boldsymbol{d}}_b$ and $\hat{\boldsymbol{d}}_h$ will ideally be a good approximation of the true chest wall motion and can, finally, be used for frequency estimation. The estimation process is responsible for detecting the breathing/heartbeat cycles and calculating their period or, alternatively, for directly estimating the dominant frequency in which they occur, i.e., the breathing and heart rates.

A. Slow-Time Phase Correlation

The larger bandwidth of mm-wave devices yields a much higher range resolution compared to other radar systems operating at lower frequencies. For instance, if operating at 77 GHz with 4 GHz of bandwidth, the range resolution is around 4 cm. This improved resolution increases the ability not only to resolve closely spaced objects but also to filter-out nearby interference. However, in these conditions, the human body is an extended target, and its energy may spread across a few adjacent range bins. Given that belly and back may also be involved in the respiration/heartbeat movement, vital sign information may eventually be detected in these additional range bins.

To exploit this and improve the SNR before estimation, we propose a novel slow-time phase correlation processing, which allows for the integration of the vital sign energy of nearby range bins, while still preserving its relevant frequency content. For achieving this, we first need to look into the correlation between displacement signals at adjacent range bins. By stacking the phase demodulated samples in the current processing window, we can define $\hat{\boldsymbol{d}}_d$ and $\hat{\boldsymbol{d}}_i$ as the vectors with the recovered displacement signals at the detected and the ith adjacent range bin, respectively. We can then calculate the Pearson correlation coefficient, given by

$$\rho(\hat{\boldsymbol{d}}_d, \hat{\boldsymbol{d}}_i) = \frac{\mathrm{cov}(\hat{\boldsymbol{d}}_d, \hat{\boldsymbol{d}}_i)}{\sigma_{\hat{\boldsymbol{d}}_d}\sigma_{\hat{\boldsymbol{d}}_i}} \tag{8}$$

where $\mathrm{cov}(\boldsymbol{d}_d, \boldsymbol{d}_i)$ represents the covariance between these vectors, with $\sigma_{\boldsymbol{d}_d}$ and $\sigma_{\boldsymbol{d}_i}$ the corresponding standard deviations. If the correlation coefficient exceeds a predetermined threshold, these displacement signals can be summed up, and the SNR will improve accordingly. This allows useful exploitation of the energy in nearby range bins, without the need of processing each one of them independently, as suggested in [26]. We can, therefore, improve estimation performance with no additional cost in terms of the computational burden.

Fig. 3 shows the effect of the slow-time phase correlation processing. The recovered displacement signals at the detected and its four adjacent are depicted in Fig. 3(a), with the corresponding calculated values for the correlation coefficient. We empirically set up a threshold value of 0.8, which, in this example, allowed the integration of three additional range bins. Fig. 3(b) shows the original phase-demodulated signal (at the detected range bin) and the enhanced signal after processing, where it can be seen how the displacement amplitude increased. In addition, the periodicity remains the same, as confirmed by looking into the spectrum in Fig. 3(c), where it is clear that the main frequency content is preserved.

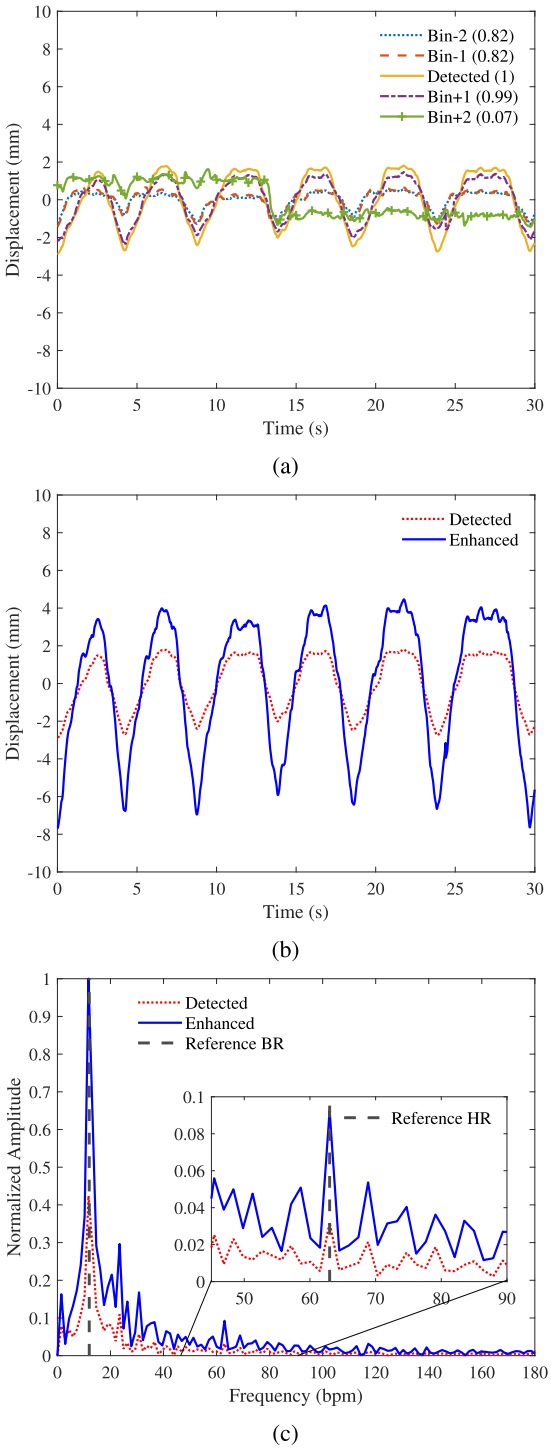

Fig. 3. Slow-time phase correlation processing. (a) Phase-demodulated displacement signals of adjacent range bins. (b) Original phase-demodulated signal (at the detected range bin) and enhanced signal after processing. (c) Spectrum of original and enhanced signals. The inset figure shows a zoom over the heartbeat frequency region. The dashed lines represent the actual breathing and heartbeat rates associated with this processing window.

The peaks corresponding to breathing and heartbeat (inset figure) have increased, and their frequencies match the true values (black dashed lines) associated with this processing window. For calculating the SNR improvement, we compared the SNR at the spectral peak location in the original (detected) displacement to the one in the enhanced signal. In this example, the obtained improvements were 3.68 and 5.45 dB for the breathing and heartbeat signals, respectively. The SNR values were calculated according to [46].

IV. Adaptive NLS Estimation

Due to the inherent periodic nature of breathing and heartbeat, any function representing these movements can eventually be decomposed into Fourier series containing the fundamental frequencies and their associated harmonics. Hence, the displacement signal can be modeled as a sum of harmonically related complex sinusoids, having frequencies that are integer multiples of the fundamental breathing/heartbeat frequency. To exploit this harmonic structure, in this section, we will use the simple NLS approach recently proposed for breathing rate estimation in [27] and [28], and extend it for heart rate estimation. For doing this, we need to take into consideration the different frequency ranges of these signals and particularly pay attention to the interference of breathing harmonics in the heartbeat signal.

A. Basic NLS Framework

The chest wall displacement signal $d(t)$ can, thus, be modeled as a superposition of K sources with L_k harmonically related complex sinusoids for the kth source, whose frequencies are integer multiples of the fundamental frequency $\omega_k > 0$. The fundamental frequencies are related to the physiological frequencies f_k (in Hertz) as $\omega_k = 2\pi(f_k/f_s)$, where f_s is the slow-time sampling frequency, which is determined by the time between transmitted frames. In addition, $f_k = 1/\tau_k$, where τ_k is the breathing/heartbeat period. After sampling for $n \in \{0, \ldots, N-1\}$, the model for the chest wall displacement signal can be written as [47]

$$d[n] = \sum_{k=1}^{K} d_k[n] = \sum_{k=1}^{K} \sum_{l=1}^{L_k} a_{k,l} e^{j\omega_k l n} \tag{9}$$

where $a_{k,l} = A_{k,l} e^{j\phi_{k,l}}$ is the complex amplitude of the lth harmonic.

Now, let us consider a single source k, and define $\boldsymbol{d}_k = [d_k[0], \ldots, d_k[N-1]]^T \in \mathbb{C}^N$, the vector consisting of N consecutive samples of $d_k[n]$, which can be expressed as

$$\boldsymbol{d}_k = \boldsymbol{Z}_k \boldsymbol{a}_k \tag{10}$$

with $\boldsymbol{a}_k = [A_{k,1} e^{j\phi_{k,1}}, \ldots, A_{k,L_k} e^{j\phi_{k,L_k}}]^T$ being the vector containing the complex amplitudes of the harmonics and the matrix $\boldsymbol{Z}_k \in \mathbb{C}^{N \times L_k}$ having a Vandermonde structure, being constructed from the L_k complex sinusoidal vectors as

$$\boldsymbol{Z}_k = [\boldsymbol{z}(\omega_k)\ \boldsymbol{z}(2\omega_k), \ldots, \boldsymbol{z}(L_k\omega_k)] \tag{11}$$

with $\boldsymbol{z}(\omega) = [1\ e^{j\omega}, \ldots, e^{j\omega(N-1)}]^T$. Using these definitions, the signal model in (9) can be rewritten as

$$\boldsymbol{d} = \sum_{k=1}^{K} \boldsymbol{Z}_k \boldsymbol{a}_k. \tag{12}$$

To obtain the NLS estimates, we look for the set of fundamental frequencies that minimize the difference between

the recovered displacement signal $\hat{\boldsymbol{d}}$ and the signal model in (12). In this way, the NLS optimization problem can be expressed as

$$\{\hat{\omega}_k\} = \arg \min_{\{\boldsymbol{a}_k\},\{\omega_k\}} \left|\left|\hat{\boldsymbol{d}} - \sum_{k=1}^{K} \boldsymbol{Z}_k \boldsymbol{a}_k\right|\right|_2^2. \tag{13}$$

Assuming that $N \gg 1$, and all frequencies in $\{\boldsymbol{Z}_k\}$ are distinct and well separated, the sources can be treated independently, and (13) can be approximated by finding the fundamental frequency of each one of them, i.e.,

$$\hat{\omega}_k = \arg \min_{\boldsymbol{a}_k,\omega_k} ||\hat{\boldsymbol{d}} - \boldsymbol{Z}_k \boldsymbol{a}_k||_2^2. \tag{14}$$

These problems are equivalent when the matrices $\{\boldsymbol{Z}_k\}$ are orthogonal, which is true asymptotically in N, as long as no harmonics overlap [47]. Minimizing (14) with respect to the complex amplitudes $\boldsymbol{a}_k$ gives amplitude estimates

$$\hat{\boldsymbol{a}}_k = \left(\boldsymbol{Z}_k^H \boldsymbol{Z}_k\right)^{-1} \boldsymbol{Z}_k^H \hat{\boldsymbol{d}} \tag{15}$$

which when inserted in (14) yields

$$\hat{\omega}_k = \arg \max_{\omega_k} \hat{\boldsymbol{d}}^H \boldsymbol{Z}_k \left(\boldsymbol{Z}_k^H \boldsymbol{Z}_k\right)^{-1} \boldsymbol{Z}_k^H \hat{\boldsymbol{d}}. \tag{16}$$

By the assumption that $N \gg 1$, we have $\boldsymbol{Z}_k^H \boldsymbol{Z}_k \approx N \cdot \boldsymbol{I}_{L_k}$, and thus,

$$\begin{aligned} \hat{\omega}_k &\approx \arg \max_{\omega_k} \hat{\boldsymbol{d}}^H \boldsymbol{Z}_k \boldsymbol{Z}_k^H \hat{\boldsymbol{d}} \\ &\approx \arg \max_{\omega_k} ||\boldsymbol{Z}_k^H \hat{\boldsymbol{d}}||_2^2. \end{aligned} \tag{17}$$

This resulting cost function can be written as

$$\sum_{l=1}^{L_k} ||z^H(\omega_k l)\hat{\boldsymbol{d}}||_2^2 \tag{18}$$

which is the periodogram power spectral density estimate of $\hat{\boldsymbol{d}}$, evaluated at and summed over the harmonic frequencies $\omega_k l$ [47]. Therefore, the NLS estimator can be efficiently implemented using an FFT algorithm and a linear grid search over the discrete candidate frequencies $\{0, (2\pi/N), \ldots, (2\pi/N)(N-1)\}$.

In this work, we are considering single dominant scatters for both breathing and heartbeat, i.e., $K = 2$. In addition, the signal models presented here are based on complex representations. As the phase-demodulated displacement signal using the AD is real, we need to map it into complex numbers.

B. Breathing Rate Estimation

The NLS objective function will exhibit peaks at the fundamental frequencies and their associated harmonics. Given the additive procedure in (18), additional peaks may also be erroneously generated at lower frequency positions. For instance, if the true breathing rate is 20 bpm, an additional peak will be generated at 10 bpm (20 bpm is a harmonic of 10 bpm), and it may have a higher amplitude than the true one at 20 bpm. To avoid detecting these additional peaks, the NLS estimator proposed in [27] and [28] uses an initial (coarse) estimation as a reference for the NLS search region, which is then limited around this value. Besides eliminating these eventual strong low-frequency components, this strategy also reduces the computational effort to perform the grid search.

In [27] and [28], this initial reference estimate is obtained using a peak detection algorithm applied directly over the time-domain displacement signal. In this work, we propose a simpler implementation for that. Given the slow variation of the breathing rate over time, instead of using an additional peak detection algorithm for calculating the reference value for the NLS search region, we can use the last NLS estimate, calculated from the previous processing window. Fig. 4(a) illustrates this idea, where f_b represents the true breathing frequency at the current (mth) processing window, and $\hat{f}_{b,m-1}$ is the previous estimate. For the first processing window, the search region is initialized over the entire physiological breathing range. For the subsequent processing windows, the search region is, thus, limited around the reference value, and it will adaptively change according to the breathing rate variation over time. In this way, besides eliminating the additional processing for calculating a new reference at each processing window, we also avoid using possible outliers as references for the current search region.

C. Heart Rate Estimation

The NLS framework does not heavily depend on the white noise assumption. In fact, when the noise is white, the NLS estimates can be interpreted as maximum likelihood estimates [48]. However, the NLS estimation performance can be affected by the nonlinear objective, with multiple peaks, and a very sharp global maximum corresponding to ω_k. Hence, finding ω_k by a search algorithm requires accurate initialization [48]. In addition, some of the assumptions made in Section IV-A may not hold in specific cases, especially considering heart rate estimation. Particularly, for preserving the signal stationarity in each processing window, the number of samples N in $\hat{\boldsymbol{d}}$ is often small and limited by the coherent processing interval (CPI). Therefore, it is not always possible to guarantee that the frequency components in $\{\boldsymbol{Z}_k\}$ are distinct and well separated. In fact, while breathing estimation is usually only limited by noise, the spectral region considering the fundamental frequency of the heartbeat is mainly dominated by breathing harmonics. In this way, spectral overlaps may occur, and the heartbeat peak may eventually be masked by breathing harmonics.

For tackling these limitations and enabling robust heart rate estimation, we extend the basic NLS approach and propose an adaptive framework for adjusting the search region over the NLS objective function. The basic idea is to generate multiple heart rate estimates based on its fundamental frequency and associated harmonics. As highlighted in [29], estimation using the fundamental heartbeat frequency (first harmonic) is mostly limited by breathing interference, whereas the estimates using higher order harmonics are only limited by noise. This is because the fundamental heartbeat frequency "competes" with still strong third-, fourth-, and fifth-order breathing harmonics. On the other hand, the second and third heartbeat harmonics, for instance, share their spectral location with strongly attenuated seventh-, eighth-, and ninth-order breathing harmonics.

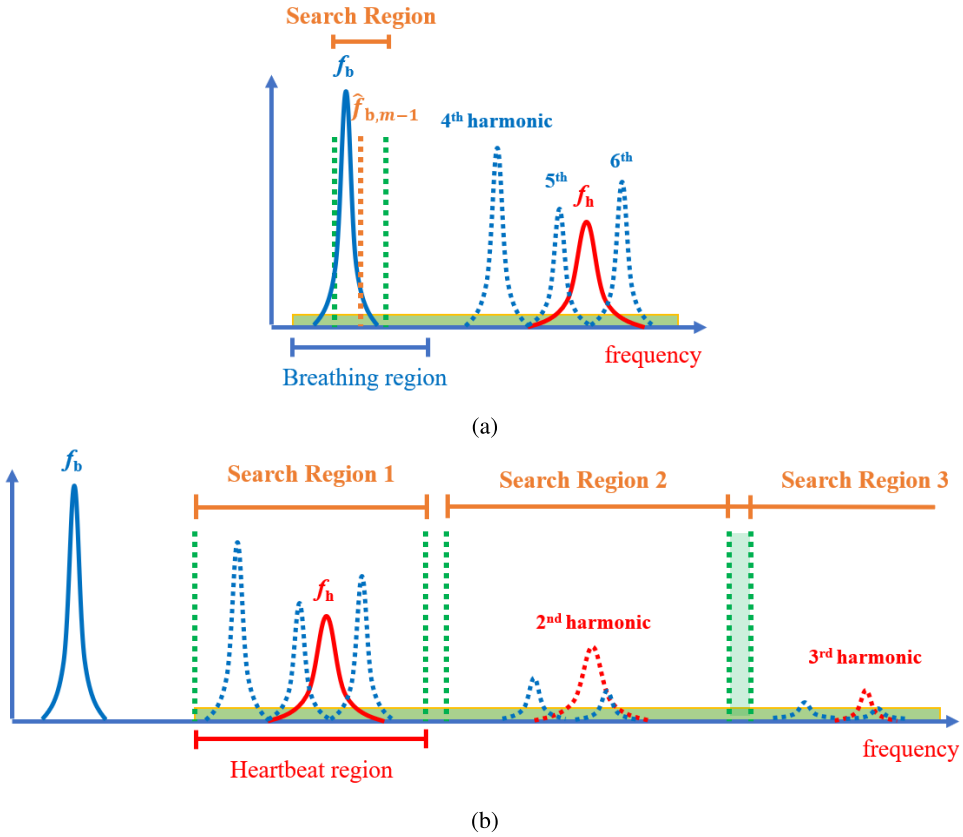

Fig. 4. Adaptive NLS framework. (a) Adaptive search region for breathing rate estimation. The search region for the current processing window is defined around the previous NLS estimate. (b) Multiple search regions for heart rate estimation. In this case, multiple estimates are calculated, and the Kalman filter stage adaptively selects among them.

The heart rate estimation can, thus, be improved if we look for its higher order harmonics, far away from the strong breathing interference. However, as the amplitude of these harmonics depends on specific characteristics of the breathing and heartbeat chest wall movements, as well as on many other processing parameters, one cannot be sure that these higher order heartbeat harmonics will always be detectable. Therefore, the conventional estimation based on the heartbeat's fundamental frequency is still needed. In this way, by simultaneously calculating multiple estimates, we increase the probability of detecting the correct peaks, and the solution becomes more robust.

The basic NLS approach can easily be extended to provide multiple estimates by simply segmenting the NLS spectrum (objective function) into different search regions and performing independent estimations (by finding the maximum value) over each of these regions. This can be done considering that, for a healthy subject at rest, the physiological range of the heart rate usually goes from 50 to 90 bpm [49]. In this way, the search region for the fundamental frequency (first harmonic) can be set up around this range. A second search region can be defined unambiguously from 100 and up to 180 bpm. Fig. 4(b) illustrates this procedure. An additional search region can also be defined, looking for the third heartbeat harmonic, from 150 to 270 bpm. However, as this third region overlaps with the second one, its estimates can be ambiguous in some cases (this issue will be handled in Section IV-D). Due to the efficient FFT-based implementation of the NLS method, we can overcome the SNR limitations reported in [29], without increasing the computation burden. In addition, this "soft" segmentation of the search regions reduces the computational complexity by only using a single bandpass filter for heartbeat estimation, in comparison to the double filtering scheme originally proposed in [29].

D. Kalman Filter Selection

The NLS method described above provides multiple heart rate estimates for the same processing window. It is, thus, necessary to come up with a single value for the heart rate estimation for each CPI. For doing this, we propose to use the Kalman filter, a recursive Bayesian algorithm that produces accurate estimates based on noisy or uncertain measurements. The Kalman filter updates its estimates and parameters sequentially as new data arrives. Therefore, it is suitable for real-time processing with the overlapped sliding windows approach commonly used for vital sign processing. As we are considering three search regions (three estimates), we can define the measurement vector as

$$z_h = \left[\hat{f}_{r1} \;\; \frac{\hat{f}_{r2}}{2} \;\; \frac{\hat{f}_{r3}}{3} \right]^T \tag{19}$$

where $\hat{f}_{r1}$, $\hat{f}_{r2}$, and $\hat{f}_{r3}$ represent the estimates originated from the first, second, and third search regions, respectively.

The generic state vector has the form

$$\boldsymbol{x} = \begin{bmatrix} f_h & f_h' & f_h'' \end{bmatrix}^T \tag{20}$$

where f_h, f_h', and f_h'' represent, respectively, the heart rate and its first and second-order derivatives. From the current state $\hat{\boldsymbol{x}}_{m,m}$, at the mth processing window, the predicted state $\hat{\boldsymbol{x}}_{m+1,m}$ can be calculated using the state transition equation, defined as

$$\hat{\boldsymbol{x}}_{m+1,m} = \begin{bmatrix} 1 & \Delta t & \frac{\Delta t^2}{2} \\ 0 & 1 & \Delta t \\ 0 & 0 & 1 \end{bmatrix} \hat{\boldsymbol{x}}_{m,m} = \boldsymbol{F}\hat{\boldsymbol{x}}_{m,m} \tag{21}$$

where $\boldsymbol{F}$ is the state transition matrix, with Δt being the time between each new set of NLS estimates. To describe the dynamics of the frequency variation over time, we are using the constant acceleration model, as suggested in [50].

The state vector represents a Gaussian process with mean $\hat{\boldsymbol{x}}_{m,m}$ and covariance $\boldsymbol{P}_{m,m}$. The extrapolated covariance can be calculated as

$$\boldsymbol{P}_{m+1,m} = \boldsymbol{F}\boldsymbol{P}_{m,m}\boldsymbol{F}^T + \boldsymbol{Q} \tag{22}$$

where $\boldsymbol{Q}$ is related to the process noise uncertainty and can be modeled as $\boldsymbol{Q} = \boldsymbol{g}\boldsymbol{g}^T\rho_a^2$ [50], with

$$\boldsymbol{g} = \begin{bmatrix} 0.5\Delta t^2 & \Delta t & 1 \end{bmatrix}^T \tag{23}$$

and ρ_a^2 representing the process noise. With the observation matrix

$$\boldsymbol{H} = \begin{bmatrix} 1 & 0 & 0 \\ 1 & 0 & 0 \\ 1 & 0 & 0 \end{bmatrix} \tag{24}$$

we can calculate the measurement innovation (error) as

$$\boldsymbol{e}_m = \boldsymbol{z}_h - \boldsymbol{H}\hat{\boldsymbol{x}}_{m+1,m} \tag{25}$$

and its associated covariance is given by

$$\boldsymbol{S}_m = \boldsymbol{H}\boldsymbol{P}_{m+1,m}\boldsymbol{H}^T + \boldsymbol{R} \tag{26}$$

with $\boldsymbol{R}$ being a diagonal matrix containing the uncertainty in the NLS estimates for each search region, i.e.,

$$\boldsymbol{R} = \begin{bmatrix} \sigma_{r1}^2 & 0 & 0 \\ 0 & \sigma_{r2}^2 & 0 \\ 0 & 0 & \sigma_{r3}^2 \end{bmatrix}. \tag{27}$$

The algorithm is initialized with predefined $\boldsymbol{Q}$ and $\boldsymbol{R}$ matrices and initial state $\hat{\boldsymbol{x}}_{0,0}$ with covariance $\boldsymbol{P}_{0,0}$. If at least one of the NLS estimates is close enough to the predicted state in (21) (within a predefined gating threshold), we select from $\boldsymbol{z}_h$ the estimate, which minimizes the distance between the new measurement and the filter prediction. Subsequently, we can update the state vector as

$$\hat{\boldsymbol{x}}_{m+1,m+1} = \hat{\boldsymbol{x}}_{m+1,m} + \boldsymbol{k}_m e_m(z) \tag{28}$$

where z is the index corresponding to the selected NLS estimate, with the Kalman gain $\boldsymbol{k}_m$ being calculated as

$$\boldsymbol{k}_m = \frac{\boldsymbol{P}_{m+1,m}\boldsymbol{h}_z}{S_m(z,z)} \tag{29}$$

where $\boldsymbol{h}_z^T$ is the zth row of $\boldsymbol{H}$ and $S_m(z,z)$ is the zth diagonal element of $\boldsymbol{S}_m$. Finally, the associated covariance

$$\boldsymbol{P}_{m+1,m+1} = \left(\boldsymbol{I} - \boldsymbol{k}_m\boldsymbol{h}_z^T\right)\boldsymbol{P}_{m+1,m} \tag{30}$$

is also calculated in order to be used in the next filter iteration.

If none of the NLS estimates fall within the gate, we treat all of them as outliers. The Kalman gain is then set to zero, and the final estimate will only be based on the predicted state. However, if this condition holds during several adjacent processing windows, it may indicate that the state estimate has diverged. In this case, we reset the updated covariance in (30) to its initial (large) value in order to allow the filter to reacquire.

The final heart rate estimate $\hat{f}_h$ for the mth processing window is directly obtained from the updated state vector in (28), and the algorithm runs for each processing window with the updated state vector, its updated covariance, and a new set of NLS estimates $\boldsymbol{z}_h$ as inputs.

At each iteration, based on its own prediction, the proposed algorithm selects the best estimate among the three NLS search regions or can even discard all of them. In this way, we are exploring the temporal information relative to the evolution of the heart rate over time. This knowledge is often neglected by previous approaches that estimate independently at each processing window. Finally, this procedure provides adaptivity to different scenarios, by avoiding wrong estimates that could be originated from harmonic-interfered spectral regions around the heartbeat fundamental frequency or from low-SNR and ambiguous detections when estimating using higher order harmonics at the second and third search regions.

V. Experimental Results

For the experiments, we are using a Texas Instruments (TI) mm-wave FMCW radar (AWR1642 [51]), operating at 79 GHz with a 4-GHz bandwidth. The radar is configured for using a single transmitter and four receiver channels. The total duration of each chirp is 64 μs, with an interframe period of 10 ms, corresponding to a slow-time sampling frequency of 100 Hz. For providing sufficient integration time, while still preserving the update rate, the data are processed using overlapped sliding windows with a duration of 30 s, with 29 s of overlap, which results in updated estimates every $\Delta t = 1$ s. The NLS search region for breathing estimation was initialized from 8 to 30 bpm and later reduced to ± 2 bpm around the reference (previous) estimate. For the heart rate estimation, the search regions were defined as described in Section IV-C. The number of harmonics for the NLS estimation was defined as $L_1 = 5$ for breathing and $L_2 = 3$ for the heart rate. The Kalman filter parameters were initialized as follows: $\rho_a = 2$, $\sigma_{r1} = \sigma_{r2} = \sigma_{r3} = 1.5$, and $\boldsymbol{P}_{0,0} = 1000\boldsymbol{I}$. The initial state is defined as $\hat{\boldsymbol{x}}_{0,0} = [4\hat{f}_b \ 0 \ 0]^T$, where $\hat{f}_b$ is the estimated breathing rate at the first processing window. This specific heart rate initialization value of $4\hat{f}_b$ is based on the human pulse-respiration quotient, which follows a log-normal distribution centered around four [52], [53].

Fig. 5(a) shows the measurement setup, where five subjects (all male) with different ages (27–36 years), height

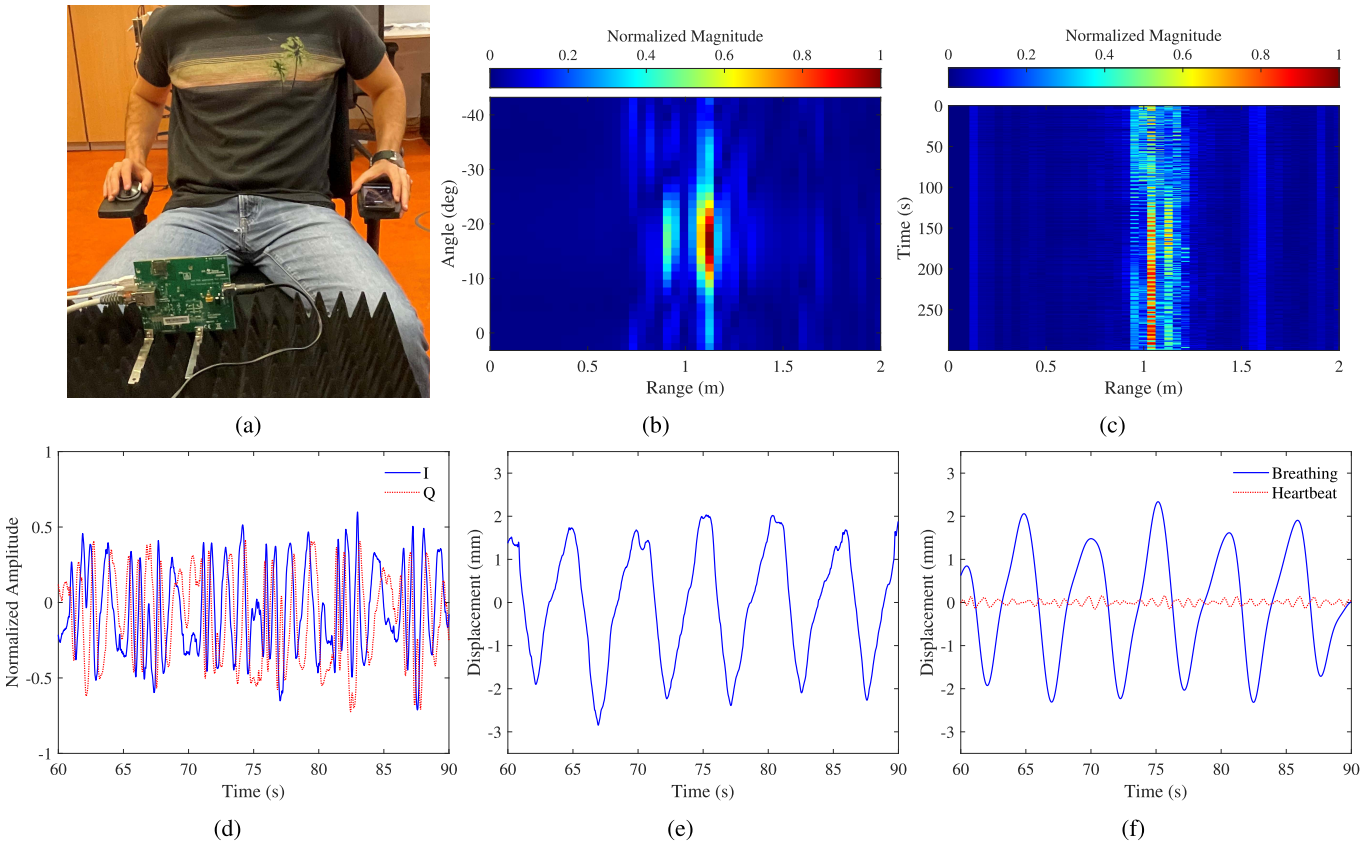

Fig. 5. Vital sign monitoring example. (a) Measurement setup, with the monitored subject seated in front of the radar, at approximately 1 m distance. (b) Range-angle map. (c) Range-profile. (d) Segment of the slow-time signal (I and Q samples) from the target range bin. (e) Phase-demodulated chest wall displacement signal. (f) Bandpass-filtered signals for breathing and heartbeat.

(170–192 cm), and weight (60–90 kg) were asked to stay seated in front of the radar, breathing normally, at approximately a 1 m distance. The wearable commercial device named Hexoskin [54] was used as a reference for true breathing and heart rates. It has two inductance plethysmography sensors (chest and abdomen) for measuring breathing and a one-lead electrocardiograph for the heartbeat. This device has already been extensively validated for vital sign monitoring in different conditions [55], [56]. The tests emulated different conditions of movement, which are common to an office work environment. The objective was to understand if small random movements from hands, arms, and shoulders, which are very close to the chest, could jeopardize estimation. Besides being static, three other scenarios were emulated: 1) holding a phone and texting; 2) typing on a keyboard; and 3) controlling a mouse device ("mousing").

Fig. 5(b) and (c) shows, respectively, the range-angle map and the range profile at the output of the preprocessing block. The energy is mostly concentrated at the detected range bin, but it also spreads over adjacent range bins due to the high range resolution. This allows us to add up correlated range bins for improving the SNR, as described in Section III. The slow-time signal (I and Q samples) at the target range bin can be seen in Fig. 5(d). After phase demodulation, the recovered chest wall displacement is depicted in Fig. 5(e), with its bandpass-filtered versions for breathing and heartbeat in Fig. 5(f). The periodic pattern is clearly seen, as well as the large-amplitude difference between the breathing and heartbeat signals.

Fig. 6(a) shows the results for a single measurement of 5 min. It compares breathing rate estimates obtained using the proposed ANLS framework, with the conventional DFT estimation [15], [18], [43] (commonly used as a benchmark), and the true values from the reference wearable device. It can be seen the high correlation between measurements with, most of the time, both techniques providing radar estimates within the $\pm$1-bpm error interval. Similarly, Fig. 6(b) compares the obtained heart rate estimates with the true values from the reference device for the same measurement of 5 min. In this case, while the proposed ANLS framework provided most estimates within the $\pm$2-bpm error interval, the conventional DFT estimation is highly affected by breathing harmonics, especially when the breathing frequency is higher.

Fig. 7(a) shows one example of the chest wall displacement signal under the influence of small random body movements ("typing" scenario). The corresponding estimation results and comparison to the reference device are depicted in Fig. 7(b). This example demonstrates the continuous nature of the emulated random body movements, which differentiates this work from previous literature [40], [57], [58], where emulated movements are short and sparse episodes. These results clearly show how the conventional DFT estimation is strongly affected

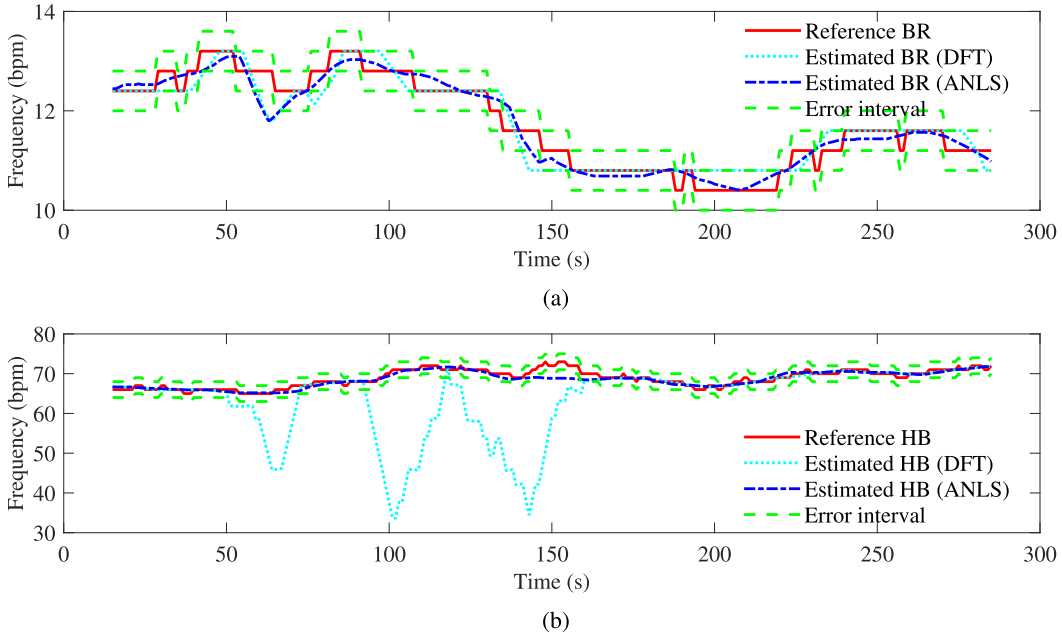

Fig. 6. Comparison between radar and reference device for a single measurement of 5 min. (a) Estimated breathing rate using conventional DFT estimation and the proposed ANLS framework, actual values from the reference device, and corresponding 1-bpm error interval. (b) Estimated heart rate using conventional DFT estimation and the proposed ANLS framework, actual values from the reference device, and corresponding 2-bpm error interval.

by the additional interference, whereas the proposed ANLS approach can still provide accurate heart rate estimation with minor performance degradation.

The obtained results are summarized in Table I, which shows the average accuracy and root mean square error (RMSE) for each scenario, comparing the proposed solution with the conventional DFT estimation, and the basic NLS approach from [28]. The same preprocessing steps (phase demodulation and bandpass filtering) were used in all cases. The accuracy is calculated as the percentage of time (in terms of processed windows) during which the final estimation from the radar is within a predefined error interval (threshold) in relation to the reference value. For instance, a 1-bpm accuracy of 80% means that the magnitude of the error between radar estimation and the reference device was smaller than 1 bpm for 80% of the time (processing windows). In this work, we considered fixed values of 1-bpm accuracy for breathing and 2-bpm accuracy for the heartbeat. These intervals are below common values for the threshold of clinical acceptance [41], [59]. The RMSE is defined as

$$\text{RMSE} = \sqrt{\frac{1}{M}\sum_{i=1}^{M}\left(\hat{f}_i - f_i\right)^2} \tag{31}$$

where $\hat{f}_i$ and f_i represent, respectively, the estimated and true (reference) frequency values (in bpm) in the ith processing window, and M is the total number of processing windows.

It can be seen how the proposed framework provides accurate and robust breathing and heart rate estimation in all conditions, with minor performance loss in the scenarios with additional movement. The most challenging situation arises when moving the arms back and forth for controlling the mouse device. Besides overlapping nearby range bins, this movement has a similar behavior as the chest wall displacement but with much stronger amplitudes.

In the case of breathing, the proposed solution provided slightly better performance compared to the conventional DFT estimation in all scenarios. The reason is that, in the absence of strong interfering movements, the breathing displacement signal already dominates the spectrum, and thus, simple DFT estimation is usually sufficient for accurate performance. In the case of heart rate estimation, due to the reduced SNR and the presence of breathing harmonics, the conventional DFT completely fails to provide accurate estimates. The proposed solution provided significant improvement over all scenarios, with the best result in the static case, with 97.6% of accuracy. The RMSE was strongly reduced in all cases, reaching the best performance with 0.76 bpm in the static scenario. The most challenging condition arises when the monitored subjects were controlling the mouse device with the accuracy reducing to 81.3% and the RMSE increasing to 2.27 bpm.

Fig. 8(a) shows the Bland–Altman plot considering the obtained ANLS breathing rate estimates for all measurements and scenarios. The mean bias was only 0.057 bpm, with 95% upper and lower limits of agreement (LOAs) of 1.1 and −0.99 bpm, respectively. These values are well within the expected interval for clinical acceptance [60]. Similarly, Fig. 8(b) shows the Bland–Altman plot considering the ANLS heart rate estimates for all measurements and scenarios. The mean bias was only 0.114 bpm with LOAs of 3.14 and −2.91 bpm. These results show very good agreement between radar estimates and the reference device, with comparable or smaller LOAs than recent studies [61], [62], [63], for both breathing and heart rate estimation.

To better evaluate the impact of the proposed ANLS solution for heart rate estimation, Fig. 9 shows the percentage of use for

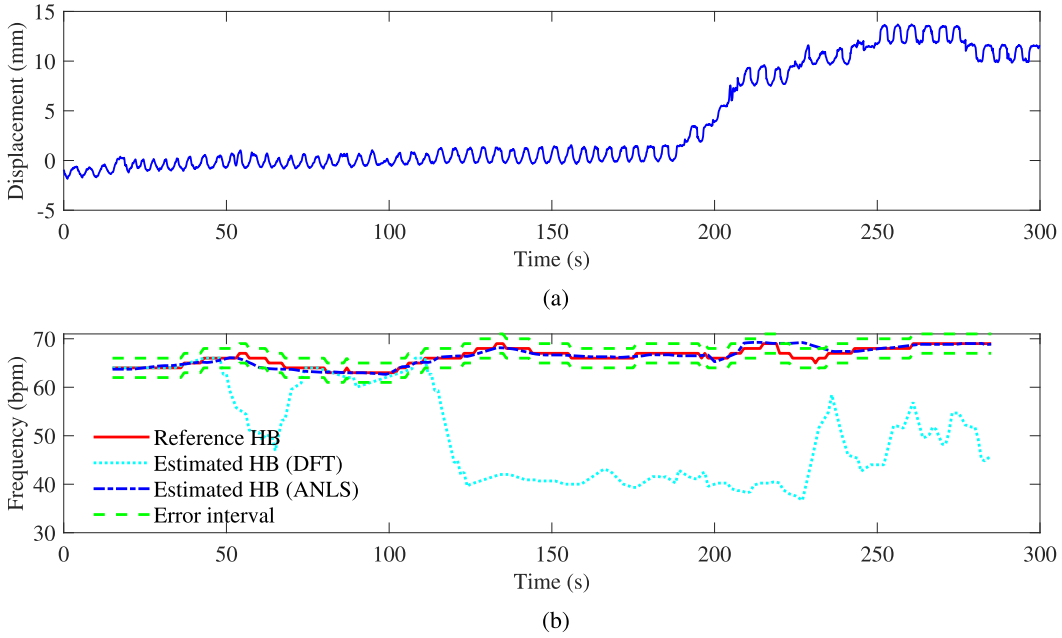

Fig. 7. Measurement under continuous interference of small random body movements ("typing" scenario). (a) Phase-demodulated chest wall displacement signal. (b) Estimated heart rate using conventional DFT estimation and the proposed ANLS framework, actual values from the reference device, and corresponding 2-bpm error interval.

TABLE I
AVERAGE ACCURACY AND RMSE FOR DIFFERENT SCENARIOS AND TECHNIQUES

Scenarios	Breathing						Heartbeat					
	Accuracy (%)			RMSE (bpm)			Accuracy (%)			RMSE (bpm)		
	DFT	NLS	ANLS	DFT	NLS	ANLS	DFT	NLS	ANLS	DFT	NLS	ANLS
Static	86.7	91.0	98.5	0.65	1.07	0.43	49.9	96.7	97.6	12.8	0.84	0.76
Texting	75.7	95.3	96.9	0.67	0.55	0.44	33.4	92.7	91.0	17.8	1.16	1.17
Typing	83.0	94.9	94.6	0.72	0.60	0.62	16.5	85.2	91.1	23.2	1.98	1.30
"Mousing"	83.2	96.8	96.8	0.71	0.57	0.52	45.4	81.0	81.3	15.4	2.50	2.27

each of the search regions [as illustrated in Fig. 4(b)]. At each processing window, the Kalman filter adaptively selects the best estimate from one of the three search regions. The main bars show the average utilization of each region considering all scenarios, whereas the error bars show the maximum and minimum values obtained in one of the measurements. Even though, most of the time, the estimate from the first region (fundamental frequency) is used, estimates from the second and third regions are used on average in 24.3% and 11.6% of the processing windows, respectively. These values rise to approximately 44% and 21%, respectively, at specific measurements. This means that, on average, more than 35% of the time the spectral region around the fundamental heartbeat frequency is dominated by breathing harmonics or any other additional interference. It confirms the significance of providing multiple estimates from different spectral regions with an additional smart mechanism to select among them.

An additional experiment was also performed at increasing distances from 1.5 to 2.5, with five measurements while seating still at each position. The obtained results are summarized in Table II, which compares the average performance for heart rate estimation in all scenarios with recently proposed solutions, validated in similar experimental conditions. It can be seen that, despite its simple implementation, the proposed ANLS framework outperforms these methods, resulting in higher accuracy and smaller RMSE values. In addition, when considering the scenarios with additional movement (texting, typing, and "mousing"), the average results show robust performance even during small and continuous body movements. Furthermore, at longer distances, despite an expected performance degradation, the results are promising with RMSE values still within thresholds of clinical acceptance [41], [59].

A. Computational Time

To estimate the computational time of the proposed approach, we processed different measurements several times and recorded the average processing time considering all scenarios. Given that we have a new processing window at every second, we can obtain an estimate of the average computational time for each iteration (processing window). We repeated this procedure using the conventional DFT estimation, the simple NLS method, and the complete ANLS approach. In relation to the conventional DFT estimation, the

TABLE II
COMPARISON OF HEART RATE ESTIMATION PERFORMANCE CONSIDERING DIFFERENT SOLUTIONS

	Device	Freq. (GHz)	Dist. (m)	RMSE (bpm)	Accuracy (%) / threshold	Scenario
[26]	FMCW	76-81	1.0	2.53	-	Seated, still
[64]	IR-UWB	7.29	1.0	2.1	-	Lying (supine), still
[65]	FMCW	8.4	1.5	> 1.0	-	Seated, still
[66]	Doppler	2.4	0.5-1.5	1.60	-	Seated, still
[67]	FMCW	60	1.0-2.5	-	85.6 / 4 bpm	Seated, still
[68]	FMCW	61	0.4-1.4	-	83.9 / 5 bpm	Seated, still
[69]	CW	2.4	1.0	-	93.8 / 2 %	Seated, still
[70]	Doppler	10.5	1.5	-	95 / 2 bpm	Seated, still
[71]	FMCW	120	1.0	-	93.7 / 3 %	Seated, still
ours	FMCW	77-81	1.0	0.76	97.6 / 2 bpm	Seated, still
			1.0	1.58	87.8 / 2 bpm	Seated, moving
			1.5	1.25	92.9 / 2 bpm	Seated, still
			2.0	1.71	87.2 / 2 bpm	Seated, still
			2.5	2.53	67.0 / 2 bpm	Seated, still

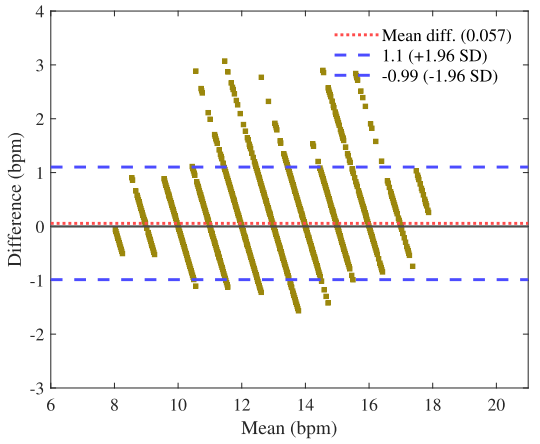

(a)

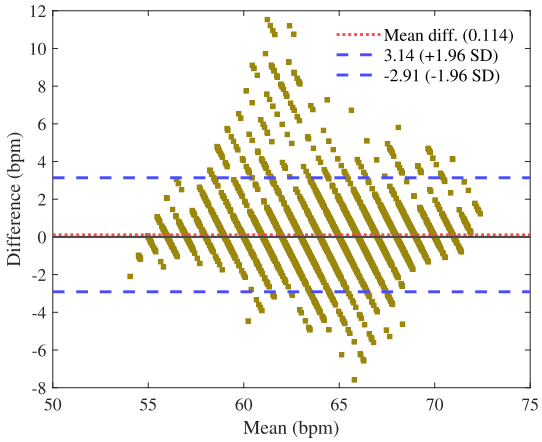

(b)

Fig. 8. Bland–Altman analysis. (a) Breathing estimation, considering all measurements. (b) Heart rate estimation, considering all measurements.

obtained results show an increase in the computational time of around 22% and 42% for the simple NLS method and the complete ANLS framework, respectively.

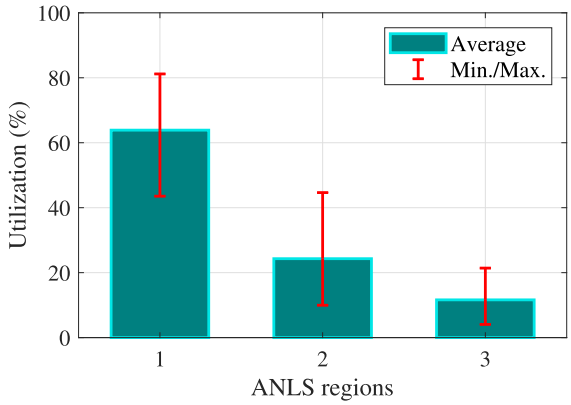

Fig. 9. Utilization of ANLS estimates from different search regions considering all measurements.

VI. CONCLUSION

In this article, we presented a complete framework for vital sign processing using a 79-GHz FMCW device. The solution is based on a simple but accurate adaptive nonlinear least squares framework that explores the inherent harmonics existing in the periodic chest wall displacement signal. In the case of heart rate estimation, an additional Kalman filter stage adaptively selects among multiple estimates originated from different search regions. The solution was evaluated with real human data collected while imitating common working conditions in an office environment. Most of the time the radar provided measurements within the predefined error intervals, being capable of tracking the reference values even during continuous small body movements. Due to the similar behavior to the chest wall movement, the most challenging scenario resulted from controlling the mouse device with back-and-forth arms movements. The final accuracy and RMSE values showed robust and accurate estimation, outperforming conventional spectral estimation and other recently proposed methods in almost all scenarios.

The proposed solution has still limitations under moderate to strong random body movements, especially when this interference leads to phase demodulation errors by using the AD. This will be the main direction of future work. Moving toward a complete solution for vital sign monitoring, additional investigation is also required to understand the effects of dynamic scenarios with multiple moving subjects and multipath reflections.

REFERENCES

[1] World Health Organization. *Ageing and Health*. Accessed: Jan. 14, 2022. [Online]. Available: https://www.who.int/news-room/fact-sheets/detail/ageing-and-health

[2] Y. Han, T. Lauteslager, T. S. Lande, and T. G. Constandinou, "UWB radar for non-contact heart rate variability monitoring and mental state classification," in *Proc. 41st Annu. Int. Conf. IEEE Eng. Med. Biol. Soc. (EMBC)*, Jul. 2019, pp. 6578–6582.

[3] V. P. Tran, A. A. Al-Jumaily, and S. M. S. Islam, "Doppler radar-based non-contact health monitoring for obstructive sleep apnea diagnosis: A comprehensive review," *Big Data Cogn. Comput.*, vol. 3, no. 1, pp. 1–21, Jan. 2019.

[4] W. Massagram, V. M. Lubecke, A. Høst-Madsen, and O. Boric-Lubecke, "Assessment of heart rate variability and respiratory sinus arrhythmia via Doppler radar," *IEEE Trans. Microw. Theory Techn.*, vol. 57, no. 10, pp. 2542–2549, Oct. 2009.

[5] J. C. Cobos-Torres, M. Abderrahim, and J. Martínez-Orgado, "Non-contact, simple neonatal monitoring by photoplethysmography," *Sensors*, vol. 18, no. 12, pp. 1–14, Dec. 2018.

[6] Y. Zhang, F. Qi, H. Lv, F. Liang, and J. Wang, "Bioradar technology: Recent research and advancements," *IEEE Microw. Mag.*, vol. 20, no. 8, pp. 58–73, Aug. 2019.

[7] M. Zakrzewski, A. Vehkaoja, A. S. Joutsen, K. T. Palovuori, and J. J. Vanhala, "Noncontact respiration monitoring during sleep with microwave Doppler radar," *IEEE Sensors J.*, vol. 15, no. 10, pp. 5683–5693, Oct. 2015.

[8] J. Li, L. Liu, Z. Zeng, and F. Liu, "Advanced signal processing for vital sign extraction with applications in UWB radar detection of trapped victims in complex environments," *IEEE J. Sel. Topics Appl. Earth Observ. Remote Sens.*, vol. 7, no. 3, pp. 783–791, Mar. 2014.

[9] D. F. Fioranelli, D. S. A. Shah, H. Li, A. Shrestha, D. S. Yang, and D. J. Le Kernec, "Radar sensing for healthcare," *Electron. Lett.*, vol. 55, no. 19, pp. 1022–1024, Sep. 2019.

[10] W. Hu, Z. Zhao, Y. Wang, H. Zhang, and F. Lin, "Noncontact accurate measurement of cardiopulmonary activity using a compact quadrature Doppler radar sensor," *IEEE Trans. Biomed. Eng.*, vol. 61, no. 3, pp. 725–735, Mar. 2014.

[11] C. Li, V. M. Lubecke, O. Boric-Lubecke, and J. Lin, "A review on recent advances in Doppler radar sensors for noncontact healthcare monitoring," *IEEE Trans. Microw. Theory Techn.*, vol. 61, no. 5, pp. 2046–2060, May 2013.

[12] J. Kranjec, S. Beguš, G. Geršak, and J. Drnovšek, "Non-contact heart rate and heart rate variability measurements: A review," *Biomed. Signal Process. Control*, vol. 13, no. 1, pp. 102–112, Sep. 2014.

[13] C. Li et al., "A review on recent progress of portable short-range noncontact microwave radar systems," *IEEE Trans. Microw. Theory Techn.*, vol. 65, no. 5, pp. 1692–1706, May 2017.

[14] G. Wang, C. Gu, T. Inoue, and C. Li, "A hybrid FMCW-interferometry radar for indoor precise positioning and versatile life activity monitoring," *IEEE Trans. Microw. Theory Techn.*, vol. 62, no. 11, pp. 2812–2822, Nov. 2014.

[15] M. Alizadeh, G. Shaker, J. C. M. De Almeida, P. P. Morita, and S. Safavi-Naeini, "Remote monitoring of human vital signs using mm-wave FMCW radar," *IEEE Access*, vol. 7, pp. 54958–54968, 2019.

[16] J. Yan, G. Zhang, H. Hong, H. Chu, C. Li, and X. Zhu, "Phase-based human target 2-D identification with a mobile FMCW radar platform," *IEEE Trans. Microw. Theory Techn.*, vol. 67, no. 12, pp. 5348–5359, Dec. 2019.

[17] J.-M. Muñoz-Ferreras, Z. Peng, R. Gómez-García, and C. Li, "Review on advanced short-range multimode continuous-wave radar architectures for healthcare applications," *IEEE J. Electromagn., RF, Microw. Med. Biol.*, vol. 1, no. 1, pp. 14–25, Jun. 2017.

[18] A. Ahmad, J. C. Roh, D. Wang, and A. Dubey, "Vital signs monitoring of multiple people using a FMCW millimeter-wave sensor," in *Proc. IEEE Radar Conf.*, Apr. 2018, pp. 1450–1455.

[19] C. Li, Y. Xiao, and J. Lin, "Experiment and spectral analysis of a low-power Ka-band heartbeat detector measuring from four sides of a human body," *IEEE Trans. Microw. Theory Techn.*, vol. 54, no. 12, pp. 4464–4471, Dec. 2006.

[20] K.-K. Shyu, L.-J. Chiu, P.-L. Lee, T.-H. Tung, and S.-H. Yang, "Detection of breathing and heart rates in UWB radar sensor data using FVPIEF-based two-layer EEMD," *IEEE Sensors J.*, vol. 19, no. 2, pp. 774–784, Jan. 2019.

[21] A. Singh, S. U. Rehman, S. Yongchareon, and P. H. J. Chong, "Multi-resident non-contact vital sign monitoring using radar: A review," *IEEE Sensors J.*, vol. 21, no. 4, pp. 4061–4084, Feb. 2021.

[22] G. Beltrao, M. Alaee-Kerahroodi, U. Schroeder, and M. R. B. Shankar, "Joint waveform/receiver design for vital-sign detection in signal-dependent interference," in *Proc. IEEE Radar Conf.*, Sep. 2020, pp. 1–6.

[23] G. Beltrão, M. Alaee-Kerahroodi, U. Schroeder, D. Tatarinov, and M. R. B. Shankar, "Statistical performance analysis of radar-based vital-sign processing techniques," in *Sensing Technology*. Cham, Switzerland: Springer, Jun. 2022, pp. 101–112.

[24] B. K. Park, O. Boric-Lubecke, and V. M. Lubecke, "Arctangent demodulation with DC offset compensation in quadrature Doppler radar receiver systems," *IEEE Trans. Microw. Theory Techn.*, vol. 55, no. 5, pp. 1073–1078, May 2007.

[25] Q. Lv et al., "Doppler vital signs detection in the presence of large-scale random body movements," *IEEE Trans. Microw. Theory Techn.*, vol. 66, no. 9, pp. 4261–4270, Sep. 2018.

[26] L. Sun et al., "Remote measurement of human vital signs based on joint-range adaptive EEMD," *IEEE Access*, vol. 8, pp. 68514–68524, 2020.

[27] G. Beltrão et al., "Contactless radar-based breathing monitoring of premature infants in the neonatal intensive care unit," *Sci. Rep.*, vol. 12, no. 1, pp. 1–15, Mar. 2022.

[28] G. Beltrao, M. Alaee-Kerahroodi, U. Schroeder, and D. Tatarinov, "Nonlinear least squares estimation for breathing monitoring using FMCW radars," in *Proc. 18th Eur. Radar Conf. (EuRAD)*, Apr. 2022, pp. 241–244.

[29] Y. Rong and D. W. Bliss, "Remote sensing for vital information based on spectral-domain harmonic signatures," *IEEE Trans. Aerosp. Electron. Syst.*, vol. 55, no. 6, pp. 3454–3465, Dec. 2019.

[30] M. Nosrati and N. Tavassolian, "High-accuracy heart rate variability monitoring using Doppler radar based on Gaussian pulse train modeling and FTPR algorithm," *IEEE Trans. Microw. Theory Techn.*, vol. 66, no. 1, pp. 556–567, Jan. 2018.

[31] A. D. Droitcour, O. Boric-Lubecke, V. M. Lubecke, J. Lin, and G. T. A. Kovacs, "Range correlation and I/Q performance benefits in single-chip silicon Doppler radars for noncontact cardiopulmonary monitoring," *IEEE Trans. Microw. Theory Techn.*, vol. 52, no. 3, pp. 838–848, Mar. 2004.

[32] U. Frey, M. Silverman, A. L. Barabási, and B. Suki, "Irregularities and power law distributions in the breathing pattern in preterm and term infants," *J. Appl. Physiol.*, vol. 85, no. 3, pp. 789–797, Sep. 1998.

[33] U. Karahasanovic, T. Stifter, H.-P. Beise, A. Fox, and D. Tatarinov, "Mathematical modelling and simulations of complex breathing patterns detected by RADAR sensors," in *Proc. 19th Int. Radar Symp. (IRS)*, Jun. 2018, pp. 1–10.

[34] J. Tu, T. Hwang, and J. Lin, "Respiration rate measurement under 1-D body motion using single continuous-wave Doppler radar vital sign detection system," *IEEE Trans. Microw. Theory Techn.*, vol. 64, no. 6, pp. 1937–1946, Jun. 2016.

[35] A. De Groote, M. Wantier, G. Cheron, M. Estenne, and M. Paiva, "Chest wall motion during tidal breathing," *J. Appl. Physiol.*, vol. 83, pp. 1531–1537, Nov. 1997.

[36] A. Albanese, L. Cheng, M. Ursino, and N. W. Chbat, "An integrated mathematical model of the human cardiopulmonary system: Model development," *Amer. J. Physiol.-Heart Circulatory Physiol.*, vol. 310, no. 7, pp. H899–H921, Apr. 2016.

[37] C. Li and J. Lin, "Random body movement cancellation in Doppler radar vital sign detection," *IEEE Trans. Microw. Theory Techn.*, vol. 56, no. 12, pp. 3143–3152, Dec. 2008.

[38] K. Naishadham, J. E. Piou, L. Ren, and A. E. Fathy, "Estimation of cardiopulmonary parameters from ultra wideband radar measurements using the state space method," *IEEE Trans. Biomed. Circuits Syst.*, vol. 10, no. 6, pp. 1037–1046, Dec. 2016.

[39] R. Qian, T. Jin, H. Li, and Y. Dai, "WT-based data-length-variation technique for fast heart rate detection," in *Proc. Prog. Electromagn. Res. Symp.*, 2018, pp. 399–404.

[40] M. Mercuri, I. R. Lorato, Y.-H. Liu, F. Wieringa, C. Van Hoof, and T. Torfs, "Vital-sign monitoring and spatial tracking of multiple people using a contactless radar-based sensor," *Nature Electron.*, vol. 2, pp. 252–262, Jun. 2019, doi: 10.1038/s41928-019-0258-6.

[41] M. Mercuri et al., "Enabling robust radar-based localization and vital signs monitoring in multipath propagation environments," *IEEE Trans. Biomed. Eng.*, vol. 68, no. 11, pp. 3228–3240, Nov. 2021.

[42] J. Tu and J. Lin, "Respiration harmonics cancellation for accurate heart rate measurement in non-contact vital sign detection," in *IEEE MTT-S Int. Microw. Symp. Dig.*, Jun. 2013, pp. 1–3.

[43] J. Tu and J. Lin, "Fast acquisition of heart rate in noncontact vital sign Radar measurement using time-window-variation technique," *IEEE Trans. Instrum. Meas.*, vol. 65, no. 1, pp. 112–122, Jan. 2016.

[44] T. Sakamoto et al., "Feature-based correlation and topological similarity for interbeat interval estimation using ultrawideband radar," *IEEE Trans. Biomed. Eng.*, vol. 63, no. 4, pp. 747–757, Apr. 2016.

[45] M. Zakrzewski et al., "Quadrature imbalance compensation with ellipse-fitting methods for microwave radar physiological sensing," *IEEE Trans. Microw. Theory Techn.*, vol. 62, no. 6, pp. 1400–1408, Jun. 2014.

[46] L. Ren, H. Wang, K. Naishadham, O. Kilic, and A. E. Fathy, "Phase-based methods for heart rate detection using UWB impulse Doppler radar," *IEEE Trans. Microw. Theory Techn.*, vol. 64, no. 10, pp. 3319–3331, Oct. 2016. [Online]. Available: http://ieeexplore.ieee.org/document/7547380/

[47] M. G. Christensen and A. Jakobsson, "Multi-pitch estimation," *Synth. Lectures Speech Audio Process.*, vol. 5, no. 1, pp. 1–160, Mar. 2009.

[48] P. Stoica et al., *Spectral Analysis of Signals*, vol. 452. London, U.K.: Pearson, May 2005.

[49] A. I. Aladin et al., "Relation of resting heart rate to risk for all-cause mortality by gender after considering exercise capacity (the Henry Ford exercise testing project)," *Amer. J. Cardiol.*, vol. 114, no. 11, pp. 1701–1706, Dec. 2014.

[50] M. Arsalan, A. Santra, and C. Will, "Improved contactless heartbeat estimation in FMCW radar via Kalman filter tracking," *IEEE Sensors Lett.*, vol. 4, no. 5, pp. 10–13, May 2020.

[51] *Radar Device*. Accessed: Oct. 28, 2020. [Online]. Available: https://www.ti.com/product/AWR1642

[52] F. Scholkmann and U. Wolf, "The pulse-respiration quotient: A powerful but untapped parameter for modern studies about human physiology and pathophysiology," *Frontiers Physiol.*, vol. 10, pp. 1–18, Apr. 2019.

[53] F. Scholkmann, H. Zohdi, and U. Wolf, "The resting-state pulse-respiration quotient of humans: Lognormally distributed and centered around a value of four," *Physiolog. Res.*, vol. 68, no. 6, pp. 1027–1032, Oct. 2019.

[54] *Hexoskin Device*. Accessed: Oct. 28, 2020. [Online]. Available: https://www.hexoskin.com/

[55] R. Villar, T. Beltrame, and R. L. Hughson, "Validation of the Hexoskin wearable vest during lying, sitting, standing, and walking activities," *Appl. Physiol., Nutrition, Metabolism*, vol. 40, no. 10, pp. 1019–1024, 2015.

[56] J. Montes, J. C. Young, R. Tandy, and J. W. Navalta, "Reliability and validation of the Hexoskin wearable bio-collection device during walking conditions," *Int. J. Exerc. Sci.*, vol. 11, no. 7, pp. 806–816, Oct. 2018.

[57] Z. K. Yang, H. Shi, S. Zhao, and X. D. Huang, "Vital sign detection during large-scale and fast body movements based on an adaptive noise cancellation algorithm using a single Doppler radar sensor," *Sensors*, vol. 20, no. 15, pp. 1–17, Jul. 2020.

[58] Q. Wu, Z. Mei, Z. Lai, D. Li, and D. Zhao, "A non-contact vital signs detection in a multi-channel 77 GHz LFMCW radar system," *IEEE Access*, vol. 9, pp. 49614–49628, 2021.

[59] M. Weenk, H. Van Goor, M. Van Acht, L. J. Engelen, T. H. Van De Belt, and J. S. Bredie, "A smart all-in-one device to measure vital signs in admitted patients," *PLoS ONE*, vol. 13, no. 2, pp. 1–12, Feb. 2018.

[60] K. van Loon, L. M. Peelen, E. C. van de Vlasakker, C. J. Kalkman, L. van Wolfswinkel, and B. van Zaane, "Accuracy of remote continuous respiratory rate monitoring technologies intended for low care clinical settings: A prospective observational study," *Can. J. Anesthesia*, vol. 65, no. 12, pp. 1324–1332, Sep. 2018, doi: 10.1007/s12630-018-1214-z.

[61] M. He, Y. Nian, L. Xu, L. Qiao, and W. Wang, "Adaptive separation of respiratory and heartbeat signals among multiple people based on empirical wavelet transform using UWB radar," *Sensors*, vol. 20, no. 17, pp. 1–17, Aug. 2020.

[62] W. H. Lee et al., "Feasibility of non-contact cardiorespiratory monitoring using impulse-radio ultra-wideband radar in the neonatal intensive care unit," *PLoS ONE*, vol. 15, no. 12, pp. 1–15, Dec. 2021, doi: 10.1371/journal.pone.0243939.

[63] T. Lauteslager, M. Maslik, F. Siddiqui, S. Marfani, G. D. Leschziner, and A. J. Williams, "Validation of a new contactless and continuous respiratory rate monitoring device based on ultra-wideband radar technology," *Sensors*, vol. 21, no. 12, p. 4027, Jun. 2021.

[64] H. Xu, M. P. Ebrahim, K. Hasan, F. Heydari, P. Howley, and M. R. Yuce, "Accurate heart rate and respiration rate detection based on a higher-order harmonics peak selection method using radar non-contact sensors," *Sensors*, vol. 22, no. 1, p. 83, Dec. 2021.

[65] Y. Xiong, Z. Peng, C. Gu, S. Li, D. Wang, and W. Zhang, "Differential enhancement method for robust and accurate heart rate monitoring via microwave vital sign sensing," *IEEE Trans. Instrum. Meas.*, vol. 69, no. 9, pp. 7108–7118, Sep. 2020.

[66] Y. Ding, X. Yu, C. Lei, Y. Sun, X. Xu, and J. Zhang, "A novel real-time human heart rate estimation method for noncontact vital sign radar detection," *IEEE Access*, vol. 8, pp. 1–11, 2020.

[67] W. Zhang, G. Li, Z. Wang, and H. Wu, "Non-contact monitoring of human heartbeat signals using mm-wave frequency-modulated continuous-wave radar under low signal-to-noise ratio conditions," *IET Radar, Sonar Navigat.*, vol. 16, no. 3, pp. 456–469, Mar. 2022.

[68] H.-I. Choi, W.-J. Song, H. Song, and H.-C. Shin, "Improved heartbeat detection by exploiting temporal phase coherency in FMCW radar," *IEEE Access*, vol. 9, pp. 163654–163664, 2021.

[69] M. Nosrati and N. Tavassolian, "Accurate Doppler radar-based cardiopulmonary sensing using chest-wall acceleration," *IEEE J. Electromagn., RF Microw. Med. Biol.*, vol. 3, no. 1, pp. 41–47, Mar. 2019.

[70] Y. Xiong, S. Chen, X. Dong, Z. Peng, and W. Zhang, "Accurate measurement in Doppler radar vital sign detection based on parameterized demodulation," *IEEE Trans. Microw. Theory Techn.*, vol. 65, no. 11, pp. 4483–4492, Nov. 2017.

[71] W. Lv, W. He, X. Lin, and J. Miao, "Non-contact monitoring of human vital signs using FMCW millimeter wave radar in the 120 GHz band," *Sensors*, vol. 21, no. 8, pp. 1–18, Apr. 2021.

Gabriel Beltrão (Graduate Student Member, IEEE) received the B.S. degree in telecommunications technology from the University of Campinas (UNICAMP), Campinas, Brazil, in 2006, the B.S. degree in electrical engineering from the University of Salvador (UNIFACS), Buenos Aires, Argentina, in 2009, and the M.S. degree from UNICAMP in 2012. He is currently pursuing the Ph.D. degree in radar signal processing at the Interdisciplinary Centre for Security, Reliability, and Trust (SnT), University of Luxembourg, Esch-sur-Alzette, Luxembourg.

Since 2011, he has been a Radar Signal Processing Engineer initially with the Radar Division of Bradar, Embraer Defense and Security, Brazil. In 2016, he joined the Special Radar Projects Group, Brazilian Army Technology Center, Brazil. Since 2019, he has been a Doctoral Researcher with SnT. His research interests include radar signal processing, waveform design, and vital sign detection and estimation with radars.

Wallace A. Martins (Senior Member, IEEE) received the Electronics Engineer degree and the M.Sc. and D.Sc. degrees in electrical engineering from the Federal University of Rio de Janeiro (UFRJ), Rio de Janeiro, Brazil, in 2007, 2009, and 2011, respectively.

He was a Research Visitor with the University of Notre Dame, Notre Dame, IN, USA, in 2008, Université de Lille 1, Villeneuve-d'Ascq, France, in 2016, and the Universidad de Alcalá, Alcala de Henares, Spain, in 2018. He was an Associate Professor with the Department of Electronics and Computer Engineering (DEL/Poli) and the Electrical Engineering Program (PEE/COPPE), UFRJ, from 2013 to 2022. He was an Academic Coordinator and the Deputy Department Chairperson (DEL/Poli) of UFRJ from 2016 to 2017. He is currently a Research Scientist with the Interdisciplinary Centre for Security, Reliability and Trust (SnT), University of Luxembourg, Esch-sur-Alzette, Luxembourg. His research interests include digital signal processing and telecommunications, with a focus on equalization and beamforming/precoding for terrestrial and nonterrestrial (satellite) wireless communications.

Dr. Martins is a member (Associate Editor) of the editorial boards of the IEEE SIGNAL PROCESSING LETTERS and the *EURASIP Journal on Advances in Signal Processing*. He was the recipient of the Best Student Paper Award from EURASIP at European Signal Processing Conference (EUSIPCO) 2009, Glasgow, U.K., the 2011 Best Brazilian D.Sc. Dissertation Award from Capes, and the Best Paper Award at International Telecommunications Symposium (SBrT) 2020, Florianópolis, Brazil.

Bhavani Shankar M. R. (Senior Member, IEEE) received M.S. and Ph.D. degrees in electrical communication engineering from the Indian Institute of Science, Bengaluru, India, in 2000 and 2007, respectively.

He worked on audio coding algorithms at Sasken Communications, Bengaluru, as a Design Engineer, from 2000 to 2001. He was a Visiting Student with the Communication Theory Group, ETH Zürich, Zürich, Switzerland, headed by Prof. Helmut Bölcskei in 2004. He was a Staff Design Engineer with Beceem Communications, Bengaluru, from 2006 to 2007, working on physical layer algorithms for WiMAX compliant chipsets. He held a post-doctoral position at the ACCESS Linnaeus Centre Signal Processing Laboratory, KTH Royal Institute of Technology, Stockholm, Sweden, from 2007 to September 2009. He joined the Interdisciplinary Centre for Security, Reliability and Trust (SnT), University of Luxembourg, Esch-sur-Alzette, Luxembourg, in October 2009, as a Research Associate, where he is currently a Research Scientist. His research interests include the design and optimization of MIMO communication systems, automotive radar and array processing, polynomial signal processing, satellite communication systems, resource allocation, game theory, and fast algorithms for structured matrices.

Dr. Shankar M. R. is also a member of the EURASIP Technical Area Committee on Theoretical and Methodological Trends in Signal Processing. He was a co-recipient of the 2014 Distinguished Contributions to Satellite Communications Award from the Satellite and Space Communications Technical Committee of the IEEE Communications Society. He is on the Executive Committee of the IEEE Benelux Joint Chapter on Communications and Vehicular Technology and serves as a Handling Editor for *Signal Processing* (Elsevier).

Mohammad Alaee-Kerahroodi (Member, IEEE) received the Ph.D. degree in telecommunication engineering from the Department of Electrical and Computer Engineering, Isfahan University of Technology, Isfahan, Iran, in 2017.

He has more than 12 years of practical experience in different radar systems, including ground surveillance, air surveillance, marine, and weather radar systems. In 2017, he joined SIGCOM, Interdisciplinary Centre for Security, Reliability and Trust (SnT), University of Luxembourg, Esch-sur-Alzette, Luxembourg, where he is working on innovative radar signal processing solutions for automotive MIMO radar systems and pursuing academic research in the area of radar waveform design and signal processing. At SnT, he is also in charge of radar lab activities and prototyping.

Udo Schroeder received the Dipl.Math. degree in applied mathematics from Christian-Albrechts-University zu Kiel, Kiel, Germany, in 2009, and the Ph.D. degree in applied mathematics from Saarland University, Saarbrücken, Germany, in 2015.

He started his Ph.D. studies at the Carl von Ossietzky Universität Oldenburg, Oldenburg, Germany. He is currently working on topics of radar signal processing, distributed sensing, and imaging at IEE S.A., Bissen, Luxembourg. He is the Principal Investigator of the research project "Distributed Collaborative Connected Electromagnetic mm-Wave Sensors" funded by the Luxembourgish Government.

Dimitri Tatarinov received the M.Sc. degree in electrical engineering from the University of Applied Sciences, Trier, Germany, in 2009, and the Ph.D. degree in mechanical engineering from the University of Duisburg-Essen, Duisburg, Germany, in 2015.

He is currently a Research and Development Engineer with IEE S.A., Bissen, Luxembourg, where, in recent years, his work is focusing on contactless vital sign monitoring techniques. He is also teaching at the University of Luxembourg, Esch-sur-Alzette, Luxembourg.